Mapping the electromagnetic field confinement in the gap of germanium nanoantennas with plasma wavelength of 4.5 micrometers

Eugenio Calandrini,[1] Tommaso Venanzi,[2] Felice Appugliese,[2] Michela Badioli,[2] Valeria Giliberti,[2,3] Leonetta Baldassarre,[2,3] Paolo Biagioni,[4] Francesco De Angelis,[1] Wolfgang M. Klesse,[5] Giordano Scappucci,[5,6] and Michele Ortolani[2]
[1]*Istituto Italiano di Tecnologia, Via Morego 30, 16163 Genova, Italy*
[2]*Dipartimento di Fisica, Sapienza University of Rome, Piazzale A. Moro 3 00185 Rome, Italy*
[3]*Center for Life and Nano Sciences, Istituto Italiano di Tecnologia, Viale Regina Elena 291, 00161 Rome, Italy*
[4]*Dipartimento di Fisica, Politecnico di Milano, P.zza Leonardo da Vinci 30, 20133 Milano, Italy*
[5]*School of Physics, University of New South Wales, 2052 Sydney, Australia*
[6]*QuTech, Delft University of Technology, Lorentzweg 1, 2628 CJ Delft, The Netherlands*

(Received 10 August 2016; accepted 6 September 2016; published online 19 September 2016)

We study plasmonic nanoantennas for molecular sensing in the mid-infrared made of heavily doped germanium, epitaxially grown with a bottom-up doping process and featuring free carrier density in excess of 10^{20} cm^{-3}. The dielectric function of the 250 nm thick germanium film is determined, and bow-tie antennas are designed, fabricated, and embedded in a polymer. By using a near-field photoexpansion mapping technique at $\lambda = 5.8\,\mu$m, we demonstrate the existence in the antenna gap of an electromagnetic energy density hotspot of diameter below 100 nm and confinement volume 10^5 times smaller than λ^3. *Published by AIP Publishing*. [http://dx.doi.org/10.1063/1.4962976]

Plasmonic nanoantenna designs are quickly evolving in the direction of practical molecular sensing applications[1] as their wavelength range is being extended from the visible towards the mid-infrared[2,3] (IR), where molecules indeed display unique spectral fingerprints (IR wavelengths λ between 2.5 μm and 25 μm). The two main features of plasmonic nanoantennas are electromagnetic field enhancement and confinement in subwavelength regions. The electromagnetic field enhancement is crucial for nonlinear[4] and second-order phenomena as the Raman effect.[5] Subwavelength confinement is critical for near-field microscopy[6] and few-molecule spectroscopy.[7] Both features depend on the nanoantenna geometry and on the dielectric function of the metal used to make the antenna $\varepsilon_m(\omega) = \varepsilon'_m(\omega) + i\varepsilon''_m(\omega)$, where $\omega = c/\lambda$ is the electromagnetic frequency. In many truly plasmonic designs, the field enhancement and confinement arise naturally at a metal/dielectric interface and are not limited to the "lightning rod" effect or to the exploitation of specific boundary conditions in sub-nm gaps; the device performances rely on having $\varepsilon'_m \approx -1$, i.e., on the break-up of the perfect electric-conductor (PEC) approximation.[8] In particular, at a metal/dielectric interface, the field confinement leads to a surface plasmon polariton (SPP) propagation wavevector k that can become much larger than that of the light in the dielectric,[8] and for a flat interface, in the limit of low losses $\varepsilon''_m \ll \varepsilon'_m$, reads

$$\frac{\mathrm{Re}(k)}{k_0} = \sqrt{\frac{\varepsilon_d \varepsilon'_m}{\varepsilon_d + \varepsilon'_m}} = \sqrt{\frac{\varepsilon_d}{1-e}}, \qquad (1)$$

where k_0 is the wavevector of light in vacuum, $\varepsilon_d \gtrsim 1$ is the dielectric constant of the material at the interface with the metal, and the parameter $e = -\varepsilon_d/\varepsilon'_m$, which vanishes for a PEC and quantifies the reduced propagation wavelength of the SPP. This reduced SPP propagation wavelength, for example, is at the basis of important predicted features, such as adiabatic compression in three-dimensions,[9,10] which is relevant for future single-molecule spectroscopy approaches in the mid-IR,[11] and it cannot be obtained in the limit $e \to 0$. The main problem encountered in extending the plasmonic field confinement to the mid-IR, therefore, is that noble metals behave very similarly to a PEC at mid-IR frequencies. This issue is not solved by using metal alloys and bad conductors that, in the mid-IR, not only display a much lower $-\varepsilon'_m$ than noble metals but also a much higher ε''_m, which makes the plasmonic oscillations overdamped, hence unsuitable for designing efficient devices.[12]

To overcome this mid-IR plasmonics challenge, in Refs. 13 and 14, it has been proposed to realize semiconductor nanoantennas out of high crystal quality, and heavily doped epitaxial layers with plasma wavelength in the mid-IR. The key requirements for the semiconductor material are: (i) a plasma wavelength λ_p slightly shorter than the wavelength λ_{vib} of the target molecular vibration that one wants to sense, so as to have $\varepsilon'_m \lesssim -1$; (ii) a thickness of the doped layer larger than the electromagnetic skin depth, so as to allow the mid-IR electric currents to flow into the antenna body; and (iii) a spatial homogeneity of the activated dopant density, so as to facilitate the plasmonic design. In Ref. 15, the n-InAs material system epitaxially grown on the GaAs wafers was employed. The observed nanoantenna resonance was at $\lambda > 10\,\mu$m; however, a large portion of the mid-IR molecular fingerprint region was excluded. Group-IV semiconductors such as Si and Ge have the potential for direct integration in microelectronic platforms,[16,17] also allowing for fast optical switching.[18,19] In n-Ge, given a conductivity effective mass $m^* = 0.12\,m_e$ and a screening constant $\varepsilon_{m,\infty} = 16$, $\lambda_p = \sqrt{m^* \varepsilon_0 \varepsilon_{m,\infty}/q_e^2 n_e} < 5\,\mu$m is expected if very high free electron concentrations n_e in excess of 10^{20} cm^{-3} are achieved (here m_e and q_e are the electron mass and charge, respectively). Nanoantennas have indeed been realized in the

n-Ge material system epitaxially grown on the Si wafers;[20] however in that case, doping levels of about $0.2 \times 10^{20}\,\mathrm{cm}^{-3}$, obtained by co-deposition of the dopant P and Ge, have still limited the nanoantenna operation at $\lambda > 11\,\mu\mathrm{m}$ with $\lambda_p = 9.3\,\mu\mathrm{m}$. Very recently,[21] a shorter $\lambda_p = 5.5\,\mu\mathrm{m}$ was reported for the ion-implanted n-Ge thin films, but no antenna structures were fabricated in that case.

In this work, we fabricated plasmonic nanoantennas on a 250 nm thick n-Ge film obtained by a bottom-up doping process that combines Ge deposition and doping from phosphorus molecules P_2 in ultra-high vacuum.[22,23] The n-Ge films obtained by this method can achieve a very high n_e in excess of $10^{20}\,\mathrm{cm}^{-3}$. The dielectric function of such "metallic" Ge was determined here by IR spectroscopy and confirms our expectation of $\lambda_p = 4.5\,\mu\mathrm{m}$. Bowtie antennas were designed, fabricated, and embedded in a polymer matrix with $\varepsilon_d \approx 2$ featuring a vibrational absorption line at $\lambda_{vib} = 5.8\,\mu\mathrm{m}$ ($1724\,\mathrm{cm}^{-1}$, Polymethylmethacrylate (PMMA) carboxylic stretching). The existence of hotspots with dimensions of the order of ≈100 nm is verified with a near-field mid-IR nanoimaging technique,[24–26] recently employed for mapping the field pattern of mid-IR nanoresonators,[25–29] in which the electromagnetic energy absorbed by the polymer molecules and/or by the nanoresonator itself is measured locally with a scanning probe tip.

The material sample structure is schematically shown in Fig. 1(a). The Ge films are obtained by the molecular beam epitaxy in a bottom up approach, where nearly-identical two-dimensional phosphorus doped layers are repeatedly stacked at short distances in the third, vertical dimension. Previous studies based on the anisotropic quantum interference electrical measurements, atom probe tomography, and density functional theory[23] have shown that the multi-layered doped region can be interpreted as a 3D volume of precisely defined thickness h where electrons coming from the 2D donor-containing layers can freely move, thus realizing a 3D metallic conductor with the homogenous electron density n_e.

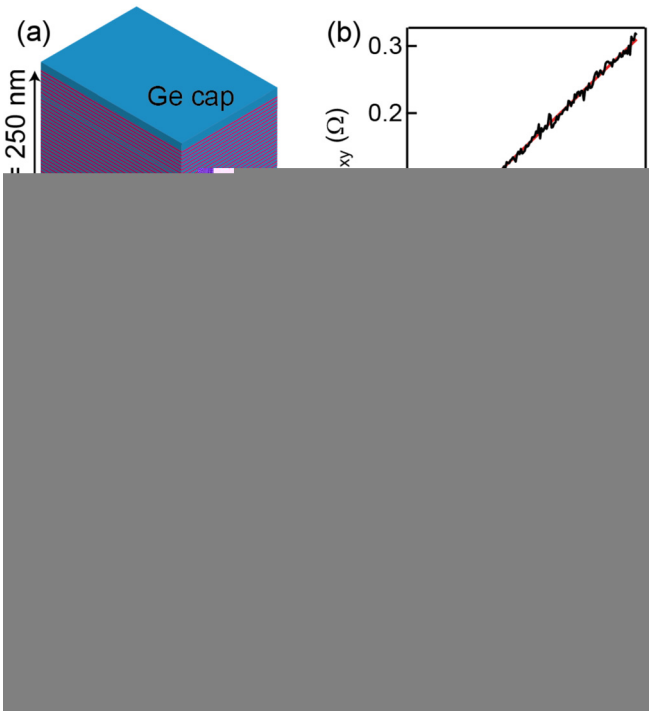

FIG. 1. (a) Schematic of the doped Ge film used for nanoantenna fabrication. The stack comprises 100 P-doped layers separated by 2.5 nm of intrinsic Ge. Each doped layer obtained by exposing the Ge (001) surface to P_2 molecules at a substrate temperature was 250 °C, leading to P incorporation into the lattice. (b) Hall effect measurement showing the linear relationship of transverse magnetoresistance ρ_{xy} vs. the perpendicular magnetic field B. The measurements were performed at $T = 4.2$ K in liquid He to freeze-out bulk conduction through the lightly doped Ge substrate. (c) IR reflectance showing the plasma edge at $\lambda_p = 4.5\,\mu\mathrm{m}$ (black line) and Drude-Lorentz fit (dashed red line). (d) IR dielectric function extracted from the fit shown in (c).

The electrical properties of the n-Ge stacks were investigated by four terminal magnetotransport measurements on the trench isolated Hall-bars using the standard low-frequency lock-in techniques. Fig. 1(b) shows the linear relationship of the transverse resistance *versus* magnetic field at low temperature T, from which a total planar density $n_{\mathrm{Hall}} = 3.4 \times 10^{15}\,\mathrm{cm}^{-2}$ is calculated, corresponding to a three-dimensional free electron density $n_e = n_{\mathrm{Hall}}/h = 1.4 \times 10^{20}\,\mathrm{cm}^{-3}$ and here $h = 250\,\mathrm{nm}$. The normal-incidence reflectance spectrum, measured by Fourier-Transform IR spectroscopy at room T, is shown in Fig. 1(c) and displays a plasma edge around 4.5 μm. The best-fit $\varepsilon_m(\omega)$ based on the Drude-Lorentz model and Fresnel relations[14] is shown in Fig. 1(d) and gives a plasma frequency $\omega_p/c = 2240\,\mathrm{cm}^{-1}$ ($\lambda_p = 4.46\,\mu\mathrm{m}$) and $n_e = 1.2 \times 10^{20}\,\mathrm{cm}^{-3}$, in good agreement with the estimate from the Hall effect. The Drude field-penetration length δ inside the conductor is determined at $\omega = \omega_p$ by the formula $\delta \approx (4\pi^2 c\omega_p)^{-1} = 113\,\mathrm{nm}$, which motivates the need for a doped film thickness $h \geq 2\delta$ with a homogeneous electrodynamic response.[30] At $\omega_{vib}/c = 1724\,\mathrm{cm}^{-1}$, for $\varepsilon_d \approx 2$, one would get a non-vanishing $e \approx 0.4$. The $\varepsilon_m(\omega)$ in Fig. 1(d) was then used as input for designing bowtie antennas by Finite-Difference Time-Domain (FDTD) electromagnetic simulations.

The choice of the bowtie nanoantenna design for the present demonstration is based on three considerations: (i) in a wire-dipole antenna with width $w \ll h$, the field penetration on the lateral walls would be longer than the antenna size, but for $w = h = 250\,\mathrm{nm}$, the antenna gap would be rather wide; (ii) if compared to linear dipoles, a triangular patch presents a hotspot at the narrower end, which is stronger and smaller than that at the broader end;[31] (iii) the bowtie antenna can be considered as two coupled triangular patches, with strong field confinement and field enhancement high enough to be measured. The final design is reported in Fig. 2. The FDTD field intensity map (Fig. 2(a)) displays a single hotspot in the gap. The three-dimensional extension of the enhanced-field volume at the antenna gap is entirely contained in a sphere of diameter $d \sim 100\,\mathrm{nm}$. The field-enhancement spectrum (Fig. 2(b)), however, is rather broad and the enhancement is not very strong, as expected for the bowtie antennas in general.[32] Antenna fabrication was carried out by focused ion beam (FIB), in which the doped material is milled at low Ga ion currents (<1 pA) with high 3D accuracy. The FIB is used here as a rapid-prototyping technique that allows to test different designs in subsequent fabrication runs on the same material sample. The representative electron microscope images acquired in the FIB chamber after fabrication are shown in Figs. 2(c) and 2(d). In order to fill the bow-tie antenna gap with a test molecular sample, the chip was spin-coated with Polymethylmethacrylate (PMMA), featuring a

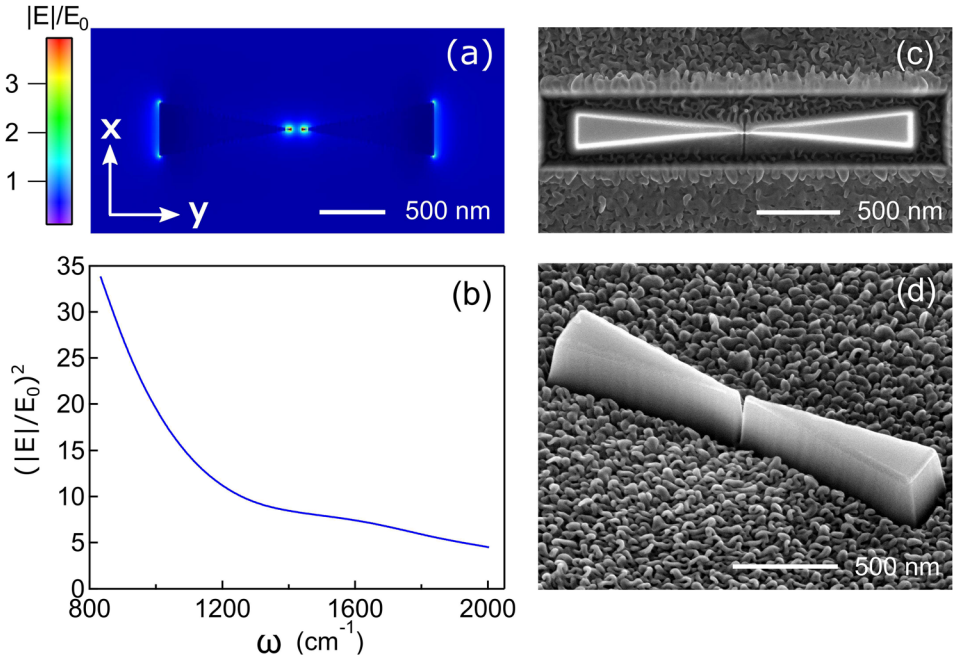

FIG. 2. (a) Electromagnetic field intensity map at the antenna surface for $\lambda = 6.0\,\mu$m, normalized to the incident plane wave amplitude E_0. The simulated triangle length is $1.0\,\mu$m, the height is 250 nm, and the apical angle is 8.5°. (b) Intensity enhancement spectrum calculated in the central hotspots visible in (a). (c) and (d) Scanning electron micrograph of two of the fabricated antennas. The fabricated triangle has the apical angle of about 7.0°, length of $1.0\,\mu$m; the structures are constituted of a 250 nm-thick Ge antenna on top of a thin (20 nm to 50 nm thick) undoped pedestal. In (c) one sees the slightly asymmetric shape of the antenna gap produced by the FIB, which has a preferential milling direction. In (d), the antenna that was investigated by IR near-field nanoimaging is shown.

strong vibrational fingerprint at $\lambda_{vib} = 5.8\,\mu$m (carbonyl bond stretch), so as to obtain a 250 nm thick PMMA film on top of the chip surface away from the antennas. As a result of the spin-coating procedure, the milled area around the antenna was filled with ~250 nm of PMMA, and the antenna surface was also coated with the PMMA.

The chip containing the nanoantennas coated with the PMMA was investigated with an atomic force microscope (AFM) featuring a near-field mid-IR microscopy function based on the resonantly enhanced photothermal expansion technique[25] (NanoIR2 by Anasys Instruments). In this version of the technique, a mid-IR quantum cascade laser is pulsed at a repetition rate matching the mechanical bending mode of the cantilever,[33] here around 180 kHz. In a contact mode, the AFM probe measures the absorbed electromagnetic energy and converted into heat by the sample, while the material under the tip expands and transfers mechanical energy to the cantilever of the AFM probe.[33,34] The resonantly enhanced amplitude of the cantilever bending oscillation (AFM-IR signal) is mapped together with the AFM topography signal by scanning the sample under the tip (Figs. 3(a) and 3(b)). Nanoscale imaging resolution can be obtained by exploiting the field-enhancement at a metal-coated tip apex providing strong T gradients in the vicinity of the tip apex.[25] In the present experiment, the electric field direction of the grazing-incidence laser beam could be rotated from almost out-of-plane (**E**//**z**) to in-plane (**E**//**x**, **E**//**y**) with a periscope, and the sample could also be rotated by 90°. We first used a gold-coated tip and **E**//**z** to quantify the actual PMMA thickness in each point of the map (Fig. 3(b)). In all the remaining imaging experiments, we used a bare silicon tip to map the field-confinement in the antenna gap with the in-plane polarization **E**//**y** (Figs. 3(c) and 3(d)). The use of the bare silicon tip is essential to avoid the interference of the field enhancement due to the gold-coating of the tip with the field pattern of the nanoantenna.[35] The maps with the **E**//**x** polarization were also acquired for reference, to eliminate the unavoidable mechanical and thermal inhomogeneity of the PMMA coating. At $\lambda_{vib} = 5.8\,\mu$m, IR absorption by the PMMA molecules generates an AFM-IR signal approximately proportional to the square of the local electric field value. In the absence of IR absorption from the PMMA (e.g., at $\lambda_0 = 6.0\,\mu$m, which we use as reference wavelength), the AFM-IR signal spectrum $S(\lambda)$ is not null because of the absorption from the tip and the antennas, which takes place at all λ, and possibly because of the radiation pressure effects on the cantilever. In order to isolate the signal contribution due to field enhancement in the gap, we define the Photoexpansion signal (PES) as

$$PES \approx \frac{S(\lambda_{vib}) - S(\lambda_0)}{S(\lambda_0)}, \tag{2}$$

which we calculate for each pixel of the maps taken at both λ_0 and λ_{vib} at **E**//**y** (resulting map shown in Fig. 3(d)) and at **E**//**x** (resulting map flat within the noise, not shown). The image in Fig. 3(d) provides a map of the nanoantenna hotspots where absorption in the PMMA is enhanced if compared to the far-field absorption that would be measured in the absence of the antenna.[28,36]

The PES map at $\lambda_{vib} = 5.8\,\mu$m in Fig. 3(d) provides a clear demonstration of enhanced energy absorption by molecules in the antenna gap. The field-confinement area matches well with the one predicted by simulations (Fig. 2(a)), as the bright spot in Fig. 3(d) is fully contained in a circle of diameter $d \sim 100$ nm. As for the z-extension of the field confinement, it is difficult to assess this quantity with the present technique, but it is certainly smaller than $h = 250$ nm. The obtained field confinement volume is then smaller than $hd^2 \approx 2.5 \times 10^{-21}\,\mathrm{m}^3$, a value 10^5 times smaller than $\lambda^3 \approx 2 \times 10^{-16}\,\mathrm{m}^3$. Finally, the field confinement can be inferred from the average line profile of Fig. 3(d) across the antenna gap, which is shown in Fig. 3(e) (red line) together with the average line profile measured with **E**//**x** (green line). The map from which the latter line profile was extracted, i.e., the analogous of the map of Fig. 3(d) but taken with **E**//**x** (not shown), did not display any indication of hotpsots. As a

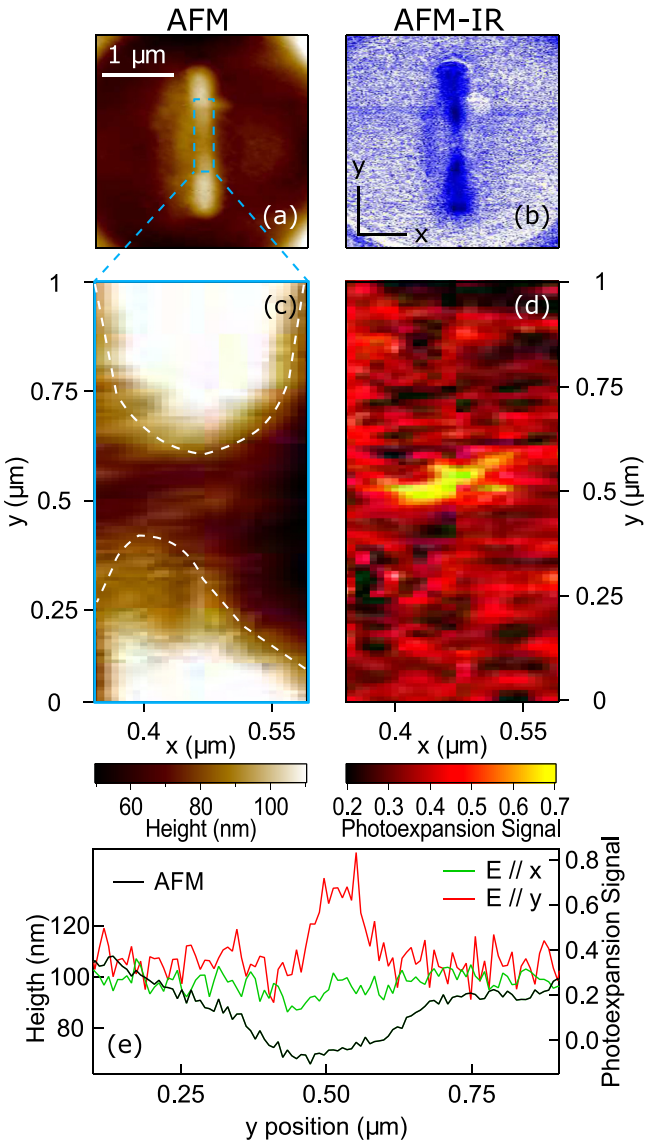

FIG. 3. ((a) and (b)) AFM height and AFM-IR signal at $\lambda_{vib} = 5.8\ \mu$m of one of the nanoantennas, after spin-coating with a PMMA layer of nominal thickness 250 nm calibrated on a flat substrate. The AFM-IR signal in (b) was acquired with a gold-coated tip and **E**//**z**, and it is proportional to the PMMA thickness (pixel brightness proportional to thickness, white corresponds to 250 nm). The nanoantenna gap is filled with ∼200 nm of PMMA and the top surface of the bow-tie triangles is coated with ∼100 nm of PMMA. ((c) and (d)) AFM height and P.E.S. calculated as from Eq. (2) from AFM-IR maps taken at high lateral resolution (10 nm) in a region of interest centered on the nanoantenna gap. The physical profile of the gap is highlighted by the dashed lines in (c), and the field-confinement hotspot is clearly seen in (d). The value of the AFM height is measured from the bare chip surface before fabrication and spin-coating of PMMA. (e) Average of the 15 line profiles taken along **y** for $0.4\ \mu m \le x \le 0.55\ \mu$m from the height in (c) (black line), the P.E.S. in (d) (red line), and the P.E.S. for **E**//**x** (map not shown, green line).

possible perspective application of the present antennas, it should be noted that the demonstrated high field confinement might enable, in conjunction with ultrashort laser pulses of high peak intensity, the generation of nonlinear effects, such as photo-bleaching and multi-photon absorption. The PES in the hotspot is 3 times higher than that outside the antenna gap, where, according to the simulation of Fig. 2(a), the field amplitude is almost equal to that of the incoming radiation field E_0. The simulation of Fig. 2(b) predicted a value of ∼7 for the electromagnetic energy density enhancement at $\omega_{vib}/c = 1724\ \text{cm}^{-1}$. This discrepancy can be attributed partly to present limitations of the fabrication process, both in terms of geometric accuracy and material damage, as also seen from the skewed physical gap profile in Fig. 3(c), and partly to the near-field mapping technique, which averages the PES from molecules inside a volume of the order of the thermal diffusion length.[24–26] Finally, it is worth noticing that, as explained in Refs. 22 and 23, the bottom-up doping process employed here is currently limited by the formation of P-P dimers, which is not a fundamental physical limitation, so it could be possible in principle to overcome the current doping level, opening the way for applications at shorter IR wavelengths. Such mid-IR Ge antennas, when compared with standard metals such as gold, feature a similar degree of confinement (mainly set by the antenna geometry in this case) and a lower local field enhancement. However, they display the advantages of higher crystal quality, easier integration in microelectronic platforms, and optical tunability of the plasma frequency of the material.

In summary, we designed and fabricated the bowtie nanoantennas made of bottom up assembled "metallic germanium" with very high free electron density of $1.2 \times 10^{20}\ \text{cm}^{-3}$ and plasma wavelength of 4.5 μm, comprising a large fraction of the mid-infrared molecular fingerprint region. In agreement with numerical simulations, we demonstrated experimentally with a near-field mapping technique the electromagnetic field confinement in hotspots with diameter of the order of 100 nm, much smaller than the mid-infrared wavelength of operation of 5.8 μm, where the vibrational absorption by molecules is enhanced by at least a factor of 3. The present results open the way to the advanced plasmonic field-confinement designs with doped semiconductors for vibrational sensing of a few molecules with mid-infrared radiation.

L.B. and M.O. acknowledge the support from the Italian Ministry of Research through program SIR (Grant No. RBSI14IT0D).

[1]B. Schwarz, P. Reininger, D. Ristanić, H. Detz, A. M. Andrews, W. Schrenk, and G. Strasser, Nat. Commun. **5**, 4085 (2014).
[2]A. E. Cetin, A. F. Coskun, B. C. Galarreta, M. Huang, D. Herman, A. Ozcan, and H. Altug, Light Sci. Appl. **3**, e122 (2014).
[3]M. Schnell, A. Garcia-Etxarri, A. J. Huber, K. Crozier, J. Aizpurua, and R. Hillenbrand, Nat. Photonics **3**, 287 (2009).
[4]M. Celebrano, X. Wu, M. Baselli, S. Großmann, P. Biagioni, A. Locatelli, C. De Angelis, G. Cerullo, R. Osellame, B. Hecht, L. Duò, F. Ciccacci, and M. Finazzi, Nat. Nanotechnol. **10**, 412 (2015).
[5]T. Yano, T. Ichimura, S. Kuwahara, F. H'Dhili, K. Uetsuki, Y. Okuno, P. Verma, and S. Kawata, Nat. Commun. **4**, 2592 (2013).
[6]M. Mivelle, T. S. van Zanten, L. Neumann, N. F. van Hulst, and M. F. Garcia-Parajo, Nano Lett. **12**, 5972 (2012).
[7]M. S. Alam, F. Karim, and C. Zhao, Nanoscale **8**, 9480 (2016).
[8]S. A. Maier, *Plasmonics: Fundamentals and Applications* (Springer, Boston, MA, USA, 2007).
[9]M. I. Stockman, Phys. Rev. Lett. **93**, 137404 (2004).
[10]V. Folli, G. Ruocco, and C. Conti, Sci. Rep. **5**, 17652 (2015).
[11]C. Huck, J. Vogt, M. Sendner, D. Hengstler, F. Neubrech, and A. Pucci, ACS Photonics **2**, 1489 (2015).
[12]G. V. Naik, V. M. Shalaev, and A. Boltasseva, Adv. Mater. **25**, 3264 (2013).
[13]S. Law, D. C. Adams, A. M. Taylor, and D. Wasserman, Opt. Express **20**, 12155 (2012).
[14]E. Calandrini, M. Ortolani, A. Nucara, G. Scappucci, W. M. Klesse, M. Y. Simmons, L. Di Gaspare, M. De Seta, D. Sabbagh, G. Capellini, M. Virgilio, and L. Baldassarre, J. Opt. **16**, 094010 (2014).

[15]S. Law, L. Yu, A. Rosenberg, and D. Wasserman, Nano Lett. **13**, 4569 (2013).
[16]J. C. Ginn, R. L. Jarecki, E. A. Shaner, and P. S. Davids, J. Appl. Phys. **110**, 043110 (2011).
[17]M. Shahzad, G. Medhi, R. E. Peale, W. R. Buchwald, J. W. Cleary, R. Soref, G. D. Boreman, and O. Edwards, J. Appl. Phys. **110**, 123105 (2011).
[18]J. Kohoutek, A. Bonakdar, R. Gelfand, D. Dey, I. Hassani Nia, V. Fathipour, O. G. Memis, and H. Mohseni, Nano Lett. **12**, 2537 (2012).
[19]M. P. Fischer, C. Schmidt, E. Sakat, J. Stock, A. Samarelli, J. Frigerio, M. Ortolani, D. J. Paul, G. Isella, A. Leitenstorfer, P. Biagioni, and D. Brida, Phys. Rev. Lett. **117**, 047401 (2016).
[20]L. Baldassarre, E. Sakat, J. Frigerio, A. Samarelli, K. Gallacher, E. Calandrini, G. Isella, D. J. Paul, M. Ortolani, and P. Biagioni, Nano Lett. **15**, 7225 (2015).
[21]S. Prucnal, F. Liu, M. Voelskow, L. Vines, L. Rebohle, D. Lang, Y. Berencén, S. Andric, R. Boettger, M. Helm, S. Zhou, and W. Skorupa, Sci. Rep. **6**, 27643 (2016).
[22]G. Mattoni, W. M. Klesse, G. Capellini, M. Y. Simmons, and G. Scappucci, ACS Nano **7**, 11310 (2013).
[23]G. Scappucci, W. M. Klesse, L. A. Yeoh, D. J. Carter, O. Warschkow, N. A. Marks, D. L. Jaeger, G. Capellini, M. Y. Simmons, and A. R. Hamilton, Sci. Rep. **5**, 12948 (2015).
[24]A. Dazzi, F. Glotin, and R. Carminati, J. Appl. Phys. **107**, 124519 (2010).
[25]F. Lu, M. Jin, and M. Belkin, Nat. Photonics **8**, 307 (2014).
[26]B. Lahiri, G. Holland, and A. Centrone, Small **9**, 439 (2013).
[27]J. R. Felts, S. Law, Ch. M. Roberts, V. Podolskiy, D. M. Wasserman, and W. P. King, Appl. Phys. Lett. **102**, 152110 (2013).
[28]B. Lahiri, G. Holland, V. Aksyuk, and A. Centrone, Nano Lett. **13**, 3218 (2013).
[29]A. B. Khanikaev, N. Arju, Z. Fan, D. Purtseladze, F. Lu, J. Lee, P. Sarriugarte, M. Schnell, R. Hillenbrand, M. A. Belkin, and G. Shvets, Nat. Commun. **7**, 12045 (2016).
[30]P. Biagioni, J.-S. Huang, and B. Hecht, Rep. Prog. Phys. **75**, 024402 (2012).
[31]S. E. Grefe, D. Leiva, S. Mastel, S. D. Dhuey, S. Cabrini, P. J. Schuck, and Y. Abate, Phys. Chem. Chem. Phys. **15**, 18944 (2013).
[32]H. Fischer and O. J. F. Martin, Opt. Express **16**, 9144 (2008).
[33]F. Lu and M. Belkin, Opt. Express **19**, 19942 (2011).
[34]J. Chae, B. Lahiri, and A. Centrone, ACS Photonics **3**, 87 (2016).
[35]A. García-Etxarri, I. Romero, F. J. García de Abajo, R. Hillenbrand, and J. Aizpurua, Phys. Rev. B **79**, 125439 (2009).
[36]J. Chae, B. Lahiri, J. Kohoutek, G. Holland, H. Lezec, and A. Centrone, Opt. Express **23**, 25912 (2015).